Frontiers of Information Technology & Electronic Engineering
www.jzus.zju.edu.cn; engineering.cae.cn; www.springerlink.com
ISSN 2095-9184 (print); ISSN 2095-9230 (online)
E-mail: jzus@zju.edu.cn

Two-bit dual-polarized reconfigurable intelligent surface with low power consumption for 6G near-field communication*

Xiaowei CAO[1,2], Changjiang DENG[†‡1,3], Youjia YIN[1], Yinan HAO[1], Weidong HU[1], Zhewei FU[4], Zhiji DENG[5]

[1]*School of Integrated Circuits and Electronics, Beijing Institute of Technology, Beijing 100081, China*

[2]*The 54th Research Institute of China Electronics Technology Group Corporation, Shijiazhuang 050081, China*

[3]*Tangshan Research Institute, Beijing Institute of Technology, Tangshan 063099, China*

[4]*Zhejiang Dahua Technology Co., Ltd., Hangzhou 310053, China*

[5]*Zhejiang Provincial Key Laboratory of Harmonized Technology of Vision & Transmission, Hangzhou 310053, China*

[†]E-mail: dengcj11@bit.edu.cn

Received May 10, 2024; Revision accepted Sept. 30, 2024; Crosschecked Nov. 6, 2024

Abstract: Near-field communication using large-scale antenna arrays is one of the hot research topics in the sixth-generation (6G) wireless communication. Reconfigurable intelligent surface (RIS) is a cost-effective method for manipulating electromagnetic waves in the near field. We propose a 2-bit dual-polarized RIS that has the merits of low cost, low power consumption, high phase accuracy, and polarization diversity. Each element consists of an aperture-coupled microstrip patch, two single-pole-four-throw (SP4T) switches, and two groups of microstrip delay lines. Two-bit phase shift is achieved by using only one SP4T switch that controls the connection of four parallel delay branches. Dual polarization is generated by placing two orthogonal slots with two 2-bit phase shifters. A 15×15 RIS prototype operating in the 3.6 GHz band is fabricated and measured. The beam can be scanned in the ±60° range, with a peak aperture efficiency of 40.1% for horizontal polarization and 38.3% for vertical polarization. What is more, the total power consumption of the RIS is merely about 100 mW, which is very attractive for massive deployment in 6G near-field communication.

Key words: Reconfigurable intelligent surface (RIS); Dual polarization; Near-field communication; 6G communication
https://doi.org/10.1631/FITEE.2400379 **CLC number:** TN82

1 Introduction

Near-field communication is a new emerging technique in the sixth-generation (6G) wireless communication, providing a higher transmission rate, lower latency, and more reliable connections. The propagation characteristics of electromagnetic (EM) waves can no longer be simply regarded as plane waves but rather as spherical waves. This introduces new EM effects such as beam splitting, polarization diversity, and evanescent waves (Li XR et al., 2022; Wang ZL et al., 2023; Zhang X and Zhang, 2023). Many traditional communication algorithms experience performance degradation in 6G near-field scenarios or are unable to fully use new features (Jiang H et al., 2023; Alexandropoulos et al., 2024; Dai ZY et al., 2024; Xu JQ et al., 2024).

The reconfigurable intelligent surface (RIS) has great potential in near-field communication because of its ability to proactively change the wireless channel environment (Wymeersch et al., 2020; Mei et al., 2022; Jiang YH et al., 2023). The waves emitted by the base station can be reprocessed by the RIS, such as beam redirection, focusing, and splitting, to enhance

‡ Corresponding author

* Project supported by the National Natural Science Foundation of China (No. 62071037)

ORCID: Xiaowei CAO, https://orcid.org/0000-0001-6071-6818; Changjiang DENG, https://orcid.org/0000-0001-6158-6437

the signal quality, fill the fading zone, and suppress the interference (Wang XH et al., 2023; Xu DN et al., 2023; Zhao, 2023). Fig. 1 shows a typical RIS-aided scenario for near-field and far-field hybrid communication. The hardware of RIS is applicable for both near-field and far-field communication. However, there are two significant differences between the two scenarios. First, the array scale of the RIS is much larger in near-field communication, to expand the near-field coverage region. Second, the beamforming algorithm is different, where the EM wave is regarded as a plane wave in far-field communication and a spherical wave in near-field communication. Due to the increase of RIS aperture, the range of near-field communication is significantly expanded, and terminal users are within the near-field region. For example, the near-field range of a RIS array with 20×20 half-wavelength-spacing elements operating at 3.6 GHz is about 22 m, and it will further increase as the array scale increases. Dense deployment of RIS is required for wide spatial coverage. Therefore, the cost and power consumption of RIS are crucial factors that will determine its massive application in the future 6G near-field communication.

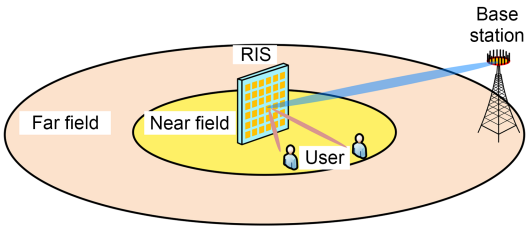

Fig. 1 Typical reconfigurable intelligent surface (RIS) aided scenario for near-field and far-field hybrid communication

The passive surface is low-cost and consumes no power, but suffers from low flexibility due to structural solidification. A RIS loaded with tunable components that can generate an agile beam is more attractive. The p-i-n diodes (Dai LL et al., 2020; Luyen et al., 2020; Lee et al., 2022; Zhang QS et al., 2022; Li P et al., 2023), varactor diodes (Hum et al., 2007; Perruisseau-Carrier, 2010; Pan et al., 2013), micro-electro-mechanical-system (MEMS) switches (Perruisseau-Carrier and Skrivervik, 2008; Moghadas et al., 2015), liquid crystal (Li XY et al., 2021; Kim et al., 2023), and graphene (Dash et al., 2022) are widely used tunable components. Among them, the p-i-n diode and MEMS switch can change the phase of cells discretely, while the varactor diode, liquid crystal, and graphene can achieve continuous phase variation at the cost of a complex biasing circuit. MEMS switches have the advantages of low insertion loss and high cut-off frequency. However, the cost and response time still have room for improvement. The p-i-n diodes make a good trade-off between cost and performance, where many commercial components are available. In addition, discrete phase quantization can approach continuous phase variation by increasing the number of quantization bits. According to the analysis of Yang et al. (2017), the phase quantization loss of 1-, 2-, and 3-bit phase discretization is 3, 0.6, and 0.2 dB, respectively. Numerous excellent RISs based on p-i-n diodes have been presented in the last decade (Han et al., 2019; Xu HJ et al., 2020; Li XR et al., 2022; Xiang et al., 2022; Wu et al., 2023). The drawback of the p-i-n diode is its high power consumption since it is current-driven. The typical biasing power of a p-i-n diode is about 0.8 W. The total power consumption of a RIS will be very large, since it usually includes hundreds of p-i-n diodes.

In this paper, a novel 2-bit dual-polarized RIS operating in the 3.6 GHz band is presented which has low power consumption. Instead of using p-i-n diodes, a single-pole-four-throw (SP4T) switch is adopted to build the 2-bit phase shifter. The complementary metal oxide semiconductor (CMOS) fabrication process gives the switch a very low biasing current. The total power consumption of the 15×15 RIS is about 100 mW. To the best of the authors' knowledge, it is the first dual-polarized RIS that uses only one tunable component to achieve a 2-bit phase shift.

2 Design of the 2-bit dual-polarized element

This section explains in detail the geometry, operating principle, and key parameters of the 2-bit dual-polarized element.

2.1 Structure of the proposed element

Fig. 2 shows the geometry and dimensions of the proposed 2-bit dual-polarized element, which is based on an aperture-coupled microstrip patch antenna. It includes two substrate layers and one metallic plate. An air gap with a height of 5 mm is inserted into the

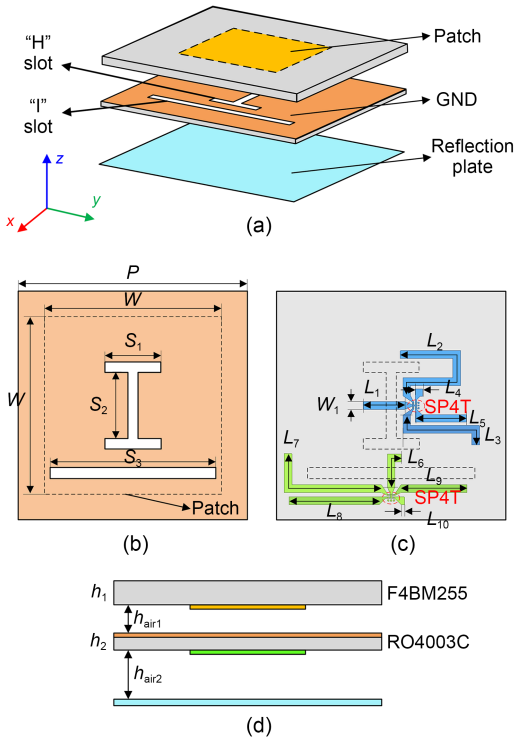

Fig. 2 Structure of the proposed 2-bit dual-polarized element: (a) 3D exploded view; (b) ground (GND) layer; (c) transmission line layer; (d) side view of the element

two substrate layers. The distance between the lower substrate layer and the metallic plate is set as 8 mm. The upper and lower substrate layers are made of F4BM255 (ε_r=2.55, tan δ=0.0015) and RO4003C (ε_r=3.55, tan δ=0.0027), respectively.

The radiating patch is printed on the bottom of the upper substrate layer. It has a square shape to support dual polarizations. The ground plane beneath the patch is printed on the top of the lower substrate layer. An H-shaped slot and an I-shaped slot are etched on the ground plane. The two slots are orthogonally placed to provide dual-polarized coupling. The microstrip transmission lines are printed on the bottom of the lower substrate layers, which can be divided into two groups. Each group has one common microstrip line and four microstrip delay branches. The common line is beneath the H-shaped or I-shaped slot to achieve EM energy coupling. The four branches have different lengths to achieve different phase delays. The connection between the common line and the four branches is controlled by an SP4T switch. By properly setting the biasing voltages, the switch can connect the common line with one of the four branches.

The center frequency point of the RIS is set as 3.6 GHz, and the operating frequency band is one of the popular sub-6 GHz bands. The period of the element is 33 mm, corresponding to 0.4 wavelengths at 3.6 GHz in the free space. All the key parameters are optimized and listed in Table 1.

Table 1 Dimensions of the proposed element

Parameter	Value (mm)	Parameter	Value (mm)
L_1	6	L_6	5.75
L_2	24.6	L_7	18.5
L_3	15.3	L_8	13
L_4	1.1	L_9	9.5
L_5	7.4	L_{10}	0.5
S_1	8	P	33
S_2	9.5	W	25.5
S_3	24	W_1	1.1
h_1	1	h_2	0.508

2.2 Phase tuning with the SP4T switch

As shown in the element structure, the tunable components are SP4T switches rather than the conventional p-i-n diodes. After investigation of the literature, it is found that the single-pole-multi-throw switch is rarely used in the RIS design. To understand the characteristics of the SP4T switch, the equivalent circuit of the switch is built, and an evaluation circuit board is fabricated and measured to extract the equivalent parameters (Vilenskiy et al., 2020; Wang EH et al., 2024).

Fig. 3 shows the equivalent circuit of the SP4T switch in the ON and OFF states. In the ON state, the SP4T switch is modeled as a series circuit of a resistor R and an inductor L, while in the OFF state, it is

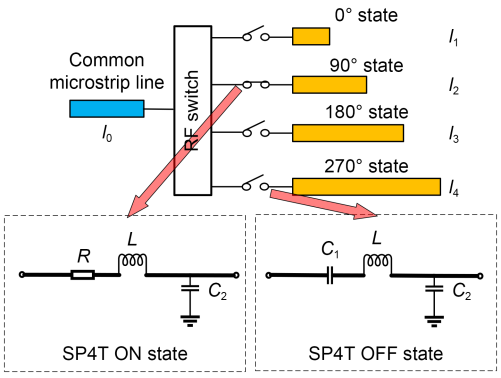

Fig. 3 Equivalent circuit of the single-pole-four-throw (SP4T) switch

modeled as a series circuit of a capacitor C_1 and an inductor L. There is a grounding capacitor C_2 in both states. The main difference between the ON and OFF states is whether a resistor or capacitor is used.

To extract the equivalent parameters of the SP4T switch, an evaluation circuit board is fabricated, as shown in Fig. 4. Considering the operating frequency, the Infineon BGSA14GN10 SP4T switch is adopted which has the merits of low cost and low power consumption. The circuit board has one signal input port and four signal output ports. Two biasing voltage pins are used to control the states of the SP4T switch. By setting high and low voltages on the two pins, the input port is connected with one output port, while the three other output ports are disconnected. The biasing circuit is simple since only binary voltage control is needed.

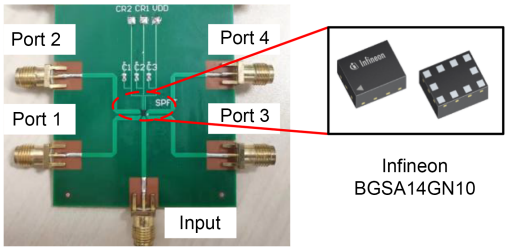

Fig. 4 Evaluation circuit board for parameter extraction of the SP4T switch

By setting the biasing voltages, port 2 is connected, while the three other output ports are disconnected. Fig. 5 compares the simulation and measurement results. The measured loss in the ON state of the SP4T switch is about 1 dB across the relevant 3.4–3.8 GHz band. In the simulation, the equivalent components are set as follows: R=1.6 Ω, C_1=120 fF, L=0.1 nH, and C_2=42 fF. It is shown that the simulation and measurement results have good consistency, indicating the feasibility of the equivalent circuit.

Based on the SP4T switch, the required 0°, 90°, 180°, and 270° states for the construction of the 2-bit phase shifter can be generated. The basic model of the element is an aperture-coupled patch with a microstrip delay line. EM wave received by the patch will first be transmitted to the microstrip line through the coupling slot. Then, it will be reflected back at the end of the microstrip line, which is open-circuited. Finally, the reflected wave will be coupled to the patch and reradiated to the free space.

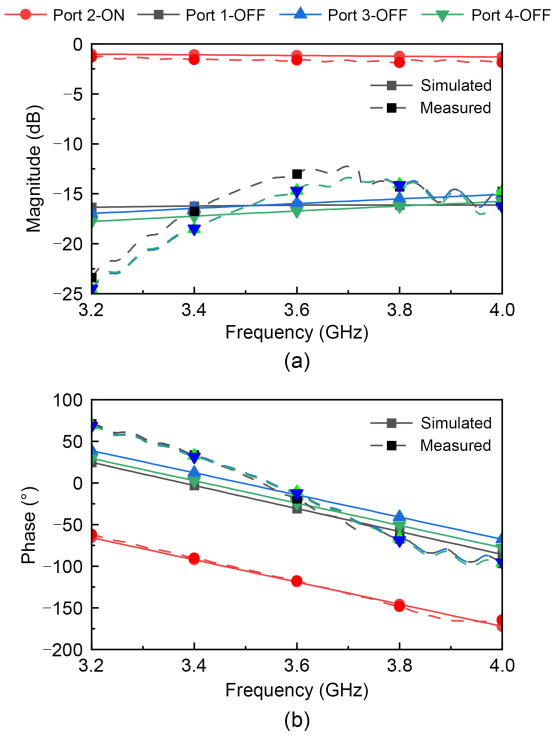

Fig. 5 Simulated and measured transmission coefficients of the evaluation board: (a) magnitude; (b) phase

The reflection phase of the element is determined mainly by the length of the microstrip delay line. According to the microwave theory, the input impedance of an open-ended transmission line can be calculated using the following equation (Yin et al., 2024):

$$Z_{\text{in}}(l)=-\text{j}Z_0\cdot\cot(\beta l), \tag{1}$$

where Z_0 is the characteristic impedance of the transmission line, β is the phase constant at 3.6 GHz, and l is the distance from the open-circuited end to the input port.

From this equation, it is known that any reflection phase could be achieved by simply changing the length of the transmission line. To achieve a dynamical phase change, switches are loaded on the transmission line. Considering the phase tuning accuracy and controlling complexity, a 2-bit phase shifter is preferred which is constructed by deploying four parallel branches with different lengths; 0°, 90°, 180°, and 270° reflection phases can be achieved by properly selecting the lengths of the four delay lines and controlling the working state of the SP4T switch.

2.3 Element performance

The proposed 2-bit dual-polarized element is simulated by using an infinite periodic boundary combined with Floquet port excitation in the Ansoft HFS software. Fig. 6 shows the simulation setup of the periodic element. The SP4T switch is modeled as a lumped component based on its equivalent circuit. Both transverse electric (TE) mode and transverse magnetic (TM) mode are excited to simulate the incident wave illumination with dual polarizations (Hao et al., 2024).

To explain the operating mechanism of the 2-bit dual-polarized element, the average current distributions on the two groups of the microstrip lines are presented in Fig. 7. Each group has one SP4T switch that controls the connection between the common line and the four parallel branches. In the left column of Fig. 7, it can be seen that the current is concentrated mainly on the line group beneath the I-shaped slot, while the intensity on the line group beneath the H-shaped slot is very weak in all four states. This means that the vertical polarization is excited independently. Furthermore, the current on the connected branch is much stronger than those on the three disconnected branches. Considering that the four branches have different lengths, four different reflection phase states are generated. By properly adjusting the lengths, the four states can provide 0°, 90°, 180°, and 270° phase shifts, corresponding to a 2-bit phase shifter. Similarly, in the right column of Fig. 7, the current distribution depicts that horizontal polarization with a 2-bit phase shifter can be excited independently. Therefore, the 2-bit dual-polarized element is constructed.

Fig. 8 shows the reflection phase and reflection magnitude of the two polarizations in the four switching states. The phase curves have good linearity among the four states in both vertical and horizontal polarizations. The reflection amplitude of the two polarizations is generally above −1 dB across the whole band in all

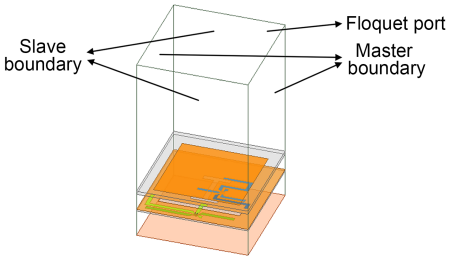

Fig. 6 Simulation setup of the periodic element

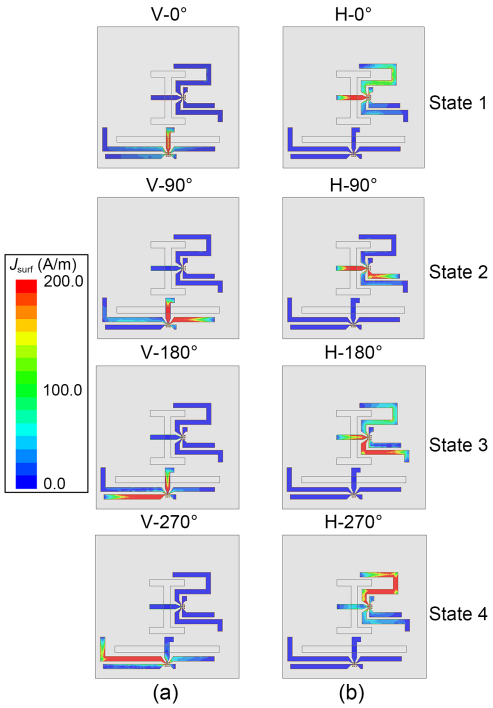

Fig. 7 Average surface current density of the four states on the microstrip lines: (a) vertical polarization; (b) horizontal polarization

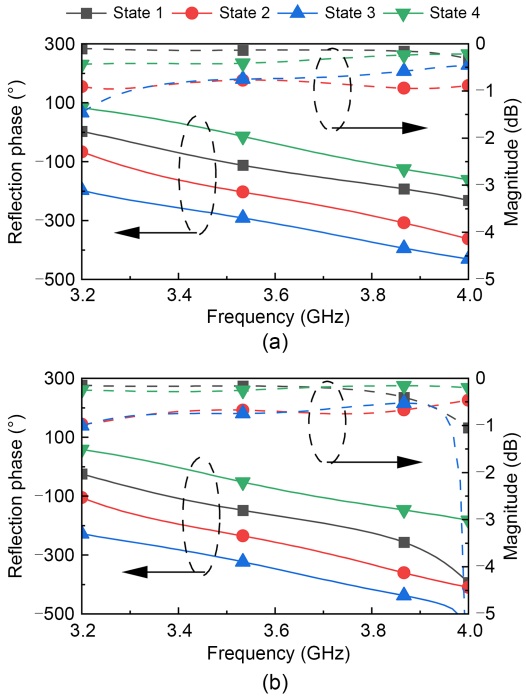

Fig. 8 Reflection phase and magnitude of the 2-bit dual-polarized element: (a) vertical polarization; (b) horizontal polarization

the states, indicating low reflection loss. It is noted that the reflection phase and loss change dramatically at 4 GHz, which is caused by the resonance of the microstrip delay line. However, since it is beyond the band concerned, this deterioration is acceptable in practical applications.

The bandwidth of the proposed 2-bit element is evaluated by using the criterion of a 90°±20° phase difference between any two adjacent phase states. Figs. 9 and 10 show the calculation results for vertical and horizontal polarizations, respectively. It is observed that the vertical and horizontal polarizations have bandwidths of 500 and 550 MHz, respectively, corresponding to 13.8% and 15.3% relative bandwidth. It is noted that the overlapping bandwidth covers the 3.4–3.8 GHz band.

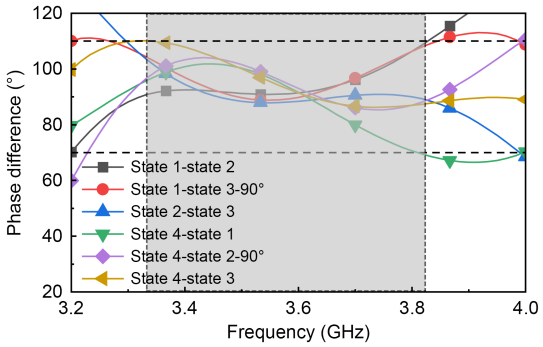

Fig. 9 Phase difference between any two adjacent states with vertical polarization

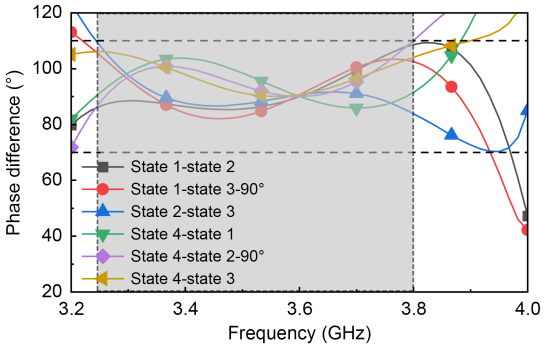

Fig. 10 Phase difference between any two adjacent states with horizontal polarization

As well as observing the current distribution in Fig. 7, the isolation between the vertical and horizontal polarizations can be further evaluated quantitatively from the coupling between any two states. As shown in Fig. 11, the simulated isolation is always greater than 27 dB within the operating frequency band, no matter which two states of the two polarizations are selected. This verifies that the proposed 2-bit element has a dual polarization feature.

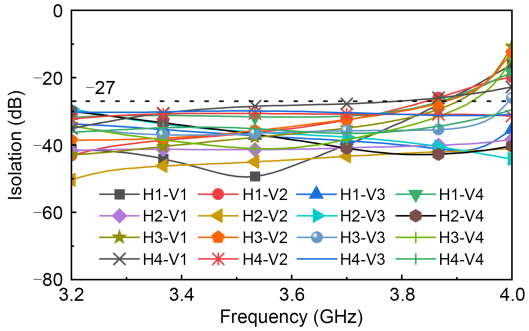

Fig. 11 Isolation between any two states between the vertical and horizontal polarizations

2.4 Parameter analysis

To optimize the performance effectively, the key parameters of the element are studied. There are two types of parameters. The first type affects only single polarization, such as the dimensions of the microstrip lines and the coupling slots. The second type affects both vertical and horizontal polarizations, such as the dimensions of the radiating patch and the thickness of the air gap.

The length of the microstrip branches is the key parameter in the first type. Take L_5 as an example; this value affects mainly state 2 in the horizontal polarization. Fig. 12 shows the influence of L_5 on the reflection phase of state 2. As L_5 increases, the phase curve shifts down with good linearity in the operating frequency bandwidth. The performances of other states are little influenced, which is not shown for brevity.

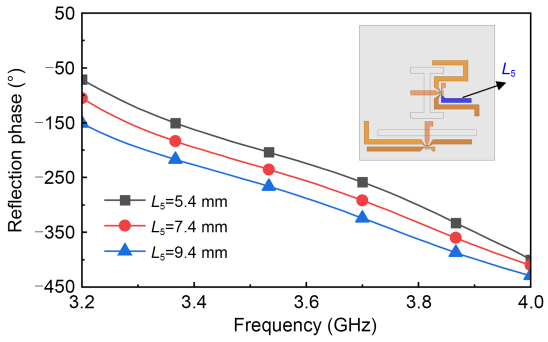

Fig. 12 Reflection phase of state 2 in horizontal polarization with different values of L_5

This implies that this type of parameter can be used to change the phase response of a single state.

The length of the common microstrip line is another key parameter in the first type. Take L_6 as an example; it can affect all the four states in the vertical polarization. Fig. 13 shows the influence of L_6 on the reflection phase of the vertical polarization. It has different influences on the four states. To be specific, state 2 and state 3 have large phase shifts when L_6 changes, while state 1 and state 4 are less sensitive. Similarly, the length of the coupling I-shaped slot (S_3) can affect all the four states. As shown in Fig. 14, state 1 and state 2 have large phase shifts when S_3 changes, while state 3 and state 4 are stable. Therefore, the two parameters are effective in optimizing multiple states of the vertical polarization.

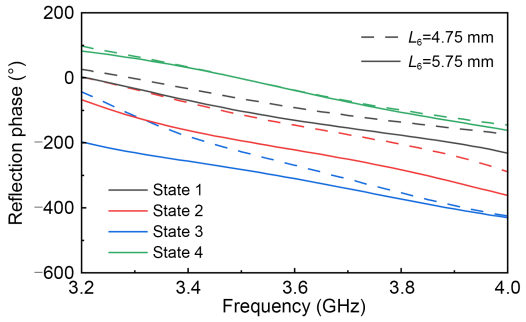

Fig. 13 Reflection phase of the four states in vertical polarization with different values of L_6 (References to color refer to the online version of this figure)

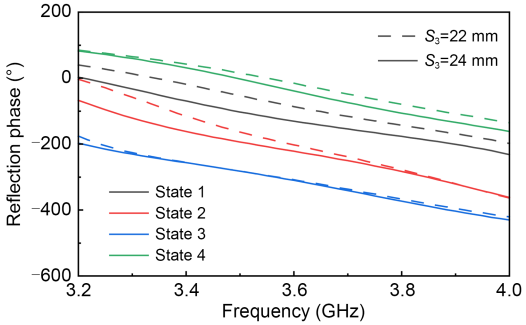

Fig. 14 Reflection phase of the four states in vertical polarization with different values of S_3 (References to color refer to the online version of this figure)

The thickness of the air gap is the key parameter in the second type. Fig. 15 shows the influence of h_{air2}, namely the distance between the lower substrate layer and the reflection plate, on the reflection phase. As h_{air2} increases, the linearity among the four curves increases, which means that the band is wider with a thicker air gap. This parameter can be used to optimize the bandwidth.

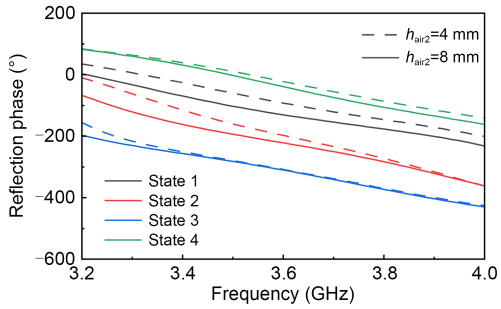

Fig. 15 Reflection phase of the four states in vertical polarization with different values of h_{air2} (References to color refer to the online version of this figure)

From the parametric study, it is known that the proposed design is very flexible in optimizing the performances of the 2-bit element.

Considering that the RIS could be illuminated from different incident angles, the angle sensitivity of the element is analyzed. Fig. 16 shows the states of the vertical polarization with different incident angles. It is seen that the linearity of the curves worsens when the incident angle moves away from 30°, which is a compromise among the multiple angles.

3 Design and measurement of RIS

A 15×15 2-bit dual-polarized RIS is designed to verify the beam scanning performances based on the proposed element. Fig. 17 shows the simulation setup of the RIS. A linearly-polarized pyramidal horn antenna with 14.5 dBi gain at 3.6 GHz is employed as the feeder. To reduce the blocking of the reflecting wave, the feed horn is located in the *xoz* plane with an oblique angle θ of 30° to the normal direction.

The feed location is an important parameter to optimize the aperture efficiency. For a horn antenna, the phase center can be easily calculated which is viewed as the equivalent point source of radiation. The height of the feeder is related to the beamwidth of the horn antenna. Fig. 18 shows the influence of the focal length to diameter (F/D) value on efficiency. When the F/D value increases, the irradiation efficiency

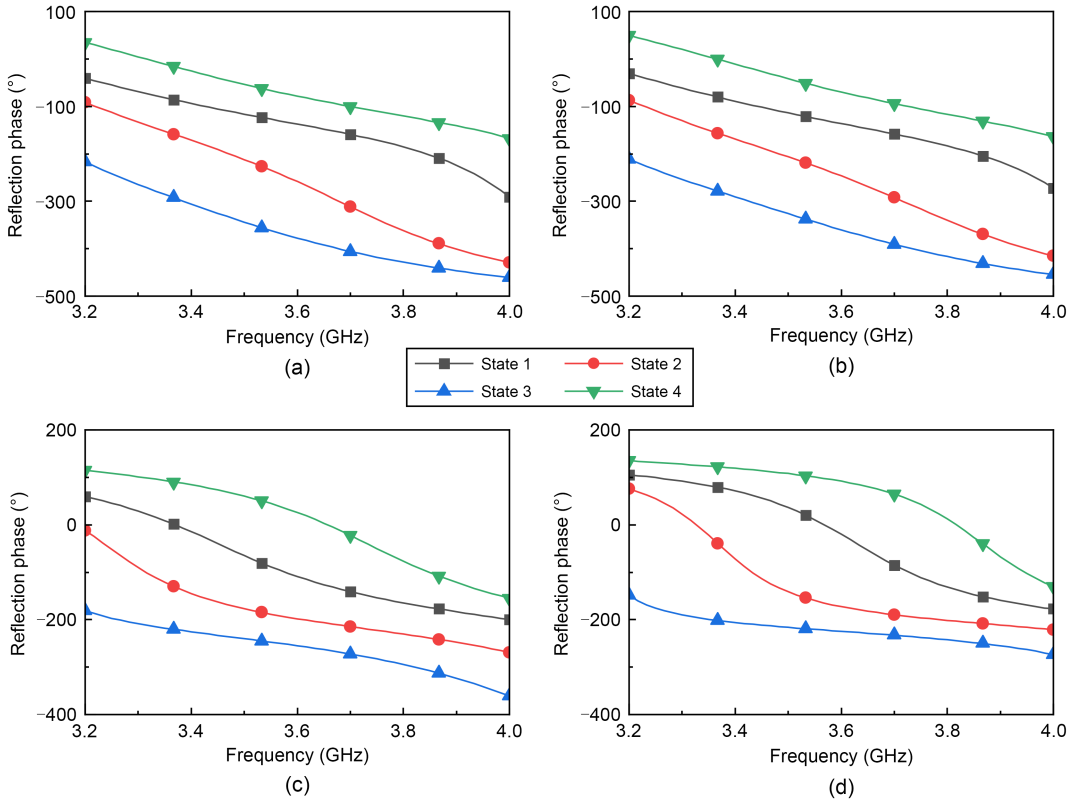

Fig. 16 Reflection phase of the four states in the vertical polarization at different oblique incident angles: (a) 0°; (b) 15°; (c) 45°; (d) 60°

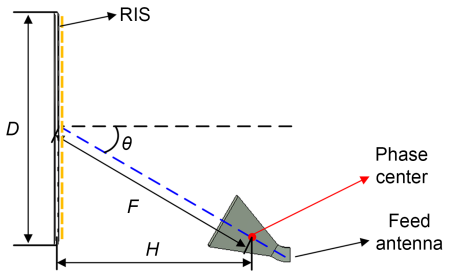

Fig. 17 Simulation model of the 15×15 RIS fed by a horn antenna

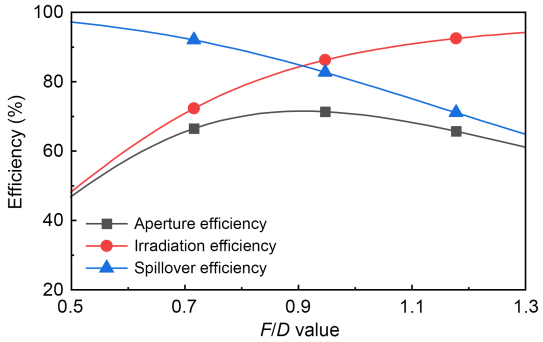

Fig. 18 Calculated aperture efficiency of the RIS with different focal length to diameter (*F*/*D*) values

increases, but the spillover efficiency decreases. Taking the two effects into consideration, the aperture efficiency is maximized if the *F*/*D* value is set as 0.9.

The change process of the RIS with beam direction is described as follows: First, set the specific beam direction (θ_0, φ_0) of the RIS as needed. Calculate the phase distribution on the aperture of the RIS according to the beam direction. The required phase compensation of each unit cell can then be obtained. Then, discrete the phase of each unit cell by using 2-bit phase quantization. Finally, set the required biasing voltage of each unit cell through the field programmable gate array (FPGA) control circuit board. In this way, the state of each antenna can change to generate different beams.

The reference phase φ_0 of the RIS provides an additional degree of freedom to optimize the gain (Mao et al., 2015; Feng et al., 2018; Li ZP et al., 2021). It can change the phase distribution of the RIS without changing the beam direction. Fig. 19 shows the gain of the broadside beam at 3.6 GHz with the change of φ_0. The gain of the vertical and horizontal polarizations

can be improved by 1.7 dB and 1 dB, respectively, by selecting the optimized φ_0.

The RIS prototype is fabricated and measured. Fig. 20 shows the photograph of the fabricated RIS in a far-field microwave anechoic chamber. The two substrate layers are assembled with nylon screws, and the reflection metal plate is made of aluminum sheet. The air gaps between the substrate layers and the plate are guaranteed by nylon pillars. Three-dimensional printed support is used to fix the feeder on the metal plate.

A low-cost Infineon BGSA14GN10 SP4T switch is adopted which can cover the 0.1–6.0 GHz band and needs only two binary biasing voltages. An FPGA circuit board is used to control the SP4T switches, and is installed on the back side of the aluminum sheet. Given that each element includes two SP4T switches, a total of 900 independent biasing voltages are needed for the 15×15 RIS. Therefore, 8-bit shift registers are used to expand the input/output (I/O) ports of the FPGA board.

Fig. 21 illustrates the measured and simulated radiation patterns at 3.6 GHz. The beam scanning range is from −60° to 60° in the *xoz* plane and from 0° to 60° in the *yoz* plane due to symmetry. It is observed that the measured main lobes of the radiation patterns

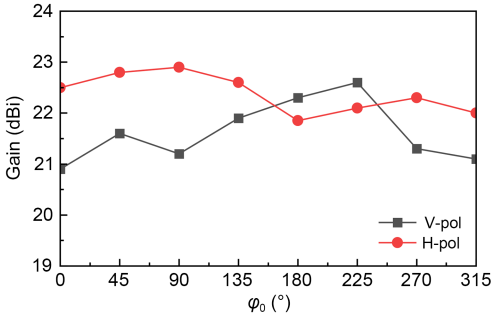

Fig. 19 Broadside gain with different reference phases φ_0 (V-pol: vertical polarization; H-pol: horizontal polarization)

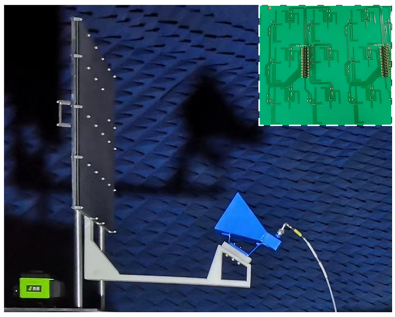

Fig. 20 Photograph of the fabricated RIS prototype in the far-field anechoic chamber

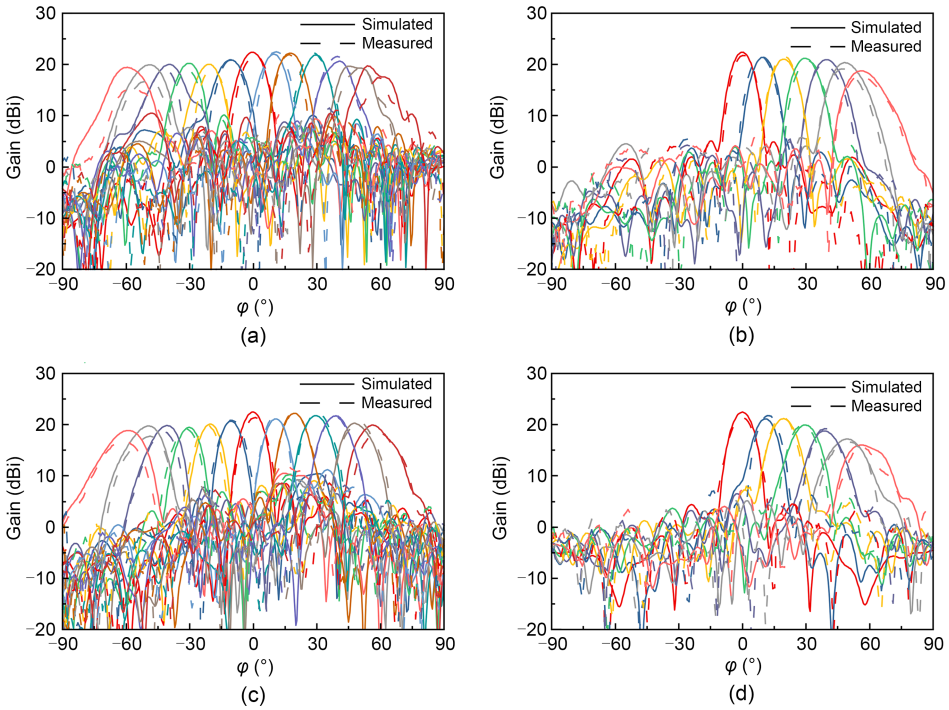

Fig. 21 Simulated and measured radiation patterns of the 2-bit dual-polarized RIS with vertical polarization in the *xoz* plane (a), vertical polarization in the *yoz* plane (b), horizontal polarization in the *xoz* plane (c), and horizontal polarization in the *yoz* plane (d)

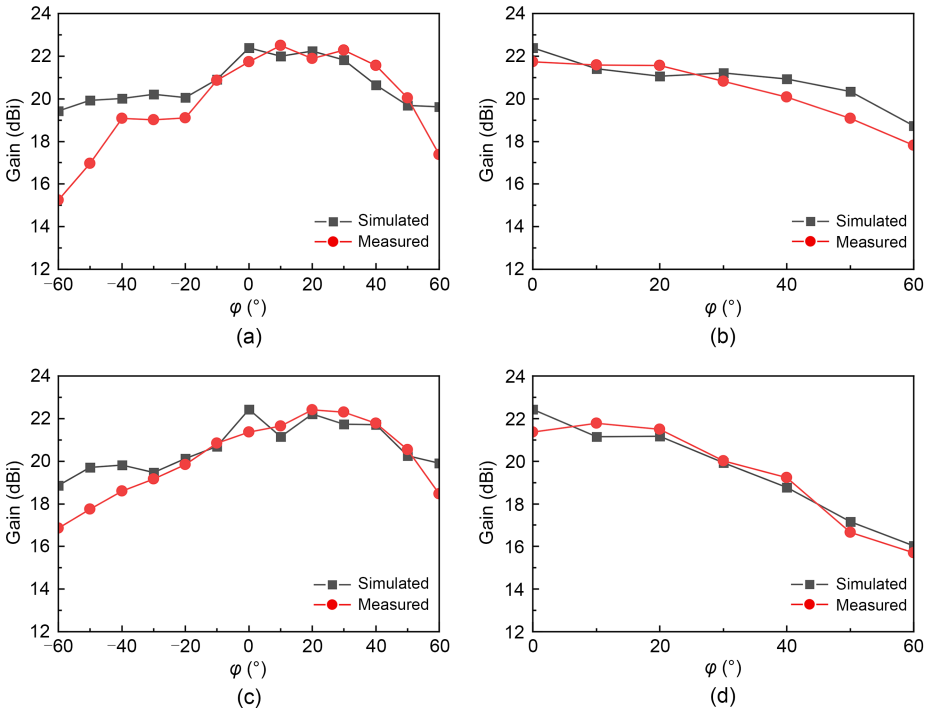

Fig. 22 Peak gain of the 2-bit dual-polarized RIS with vertical polarization in the *xoz* plane (a), vertical polarization in the *yoz* plane (b), horizontal polarization in the *xoz* plane (c), and horizontal polarization in the *yoz* plane (d)

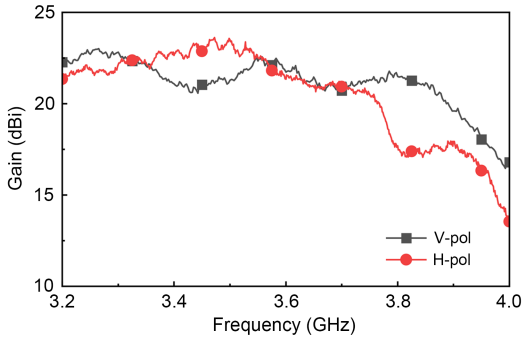

Fig. 23 Measured broadside gain of the vertical and horizontal polarizations within the operating frequency band

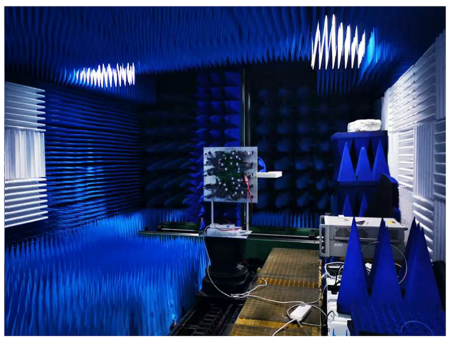

Fig. 24 Measurement setup of the RIS in the near-field anechoic chamber

agree well with the simulation results. The measured gain at the scanning angles is slightly lower than the simulation value due to fabrication errors. Fig. 22 shows the simulated and measured gains at different angles. The measured peak gain is 22.5 dBi in the *xoz* plane, corresponding to a peak aperture efficiency of 40.1%.

Fig. 23 shows the measured gain of the broadside beam with frequency variation. The peak gains of the vertical and horizontal polarizations reach 23.0 dBi and 23.6 dBi, respectively. In the 3.4–3.8 GHz band, the measured gain is above 20.5 dBi for the vertical polarization and above 17.6 dBi for the horizontal polarization.

To further evaluate the performance of the RIS, the prototype is measured in a near-field chamber, as shown in Fig. 24. The amplitude and phase distribution of different scanning beams are measured. Fig. 25 shows the results of the broadside beam. The black frame in the center is the outline of the RIS. It can be seen that most of the energy is concentrated on the RIS, and the phase fronts are close to each other in the center region.

The RIS response time is also evaluated by measuring the beam switching time. As shown in Fig. 26a, two beams with different orientations are produced by the RIS—one is pointed to the receiving antenna, and the

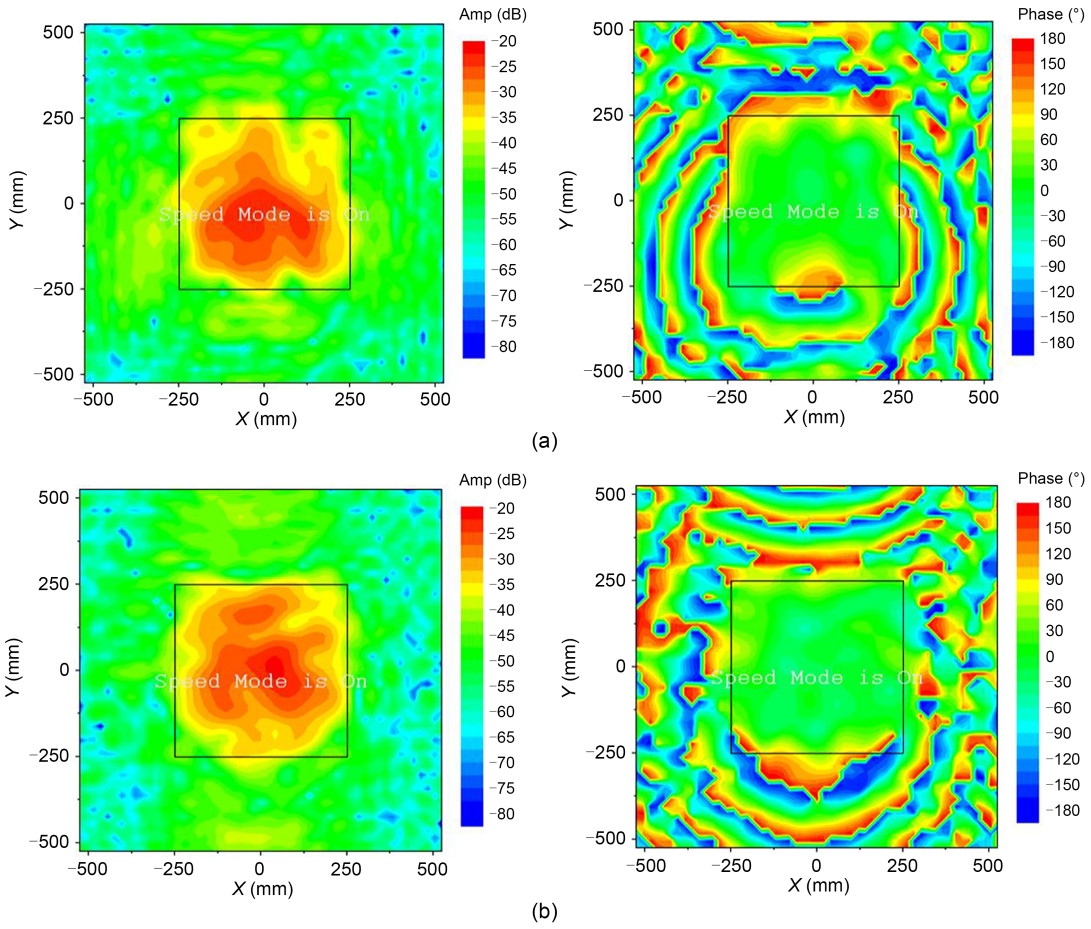

Fig. 25 Measured near-field amplitude and phase distribution of the RIS with broadside beam: (a) vertical polarization; (b) horizontal polarization

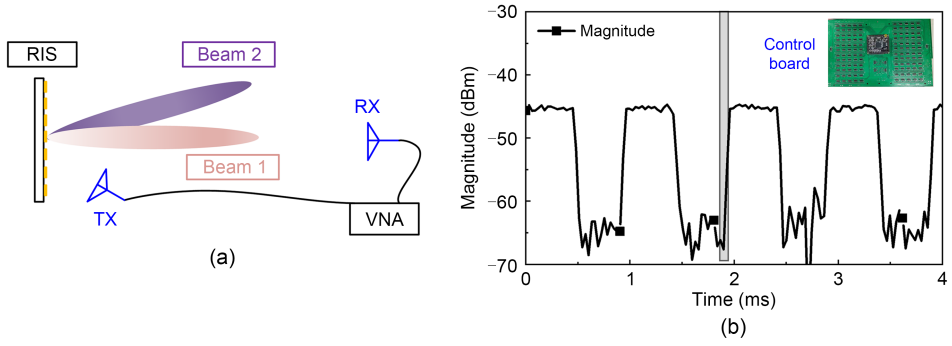

Fig. 26 Beam switching response of the proposed RIS: (a) measurement setup; (b) response time (TX: transmitter; RX: receiver; VNA: vector network analyzer)

other is not. By controlling the FPGA board, the beam is switched between the two states. High and weak intensities can be observed from the receiving signals, as shown in Fig. 26b. The rising edge from one state to the other corresponds to the response time. It can be seen that the measured response time is within 0.1 ms.

The total power consumption of the 15×15 RIS is calculated. According to the datasheet of the SP4T switch, the typical supply voltage is 2.8 V, and the supply current is 80 μA; thus, the power consumption of a single switch is 0.224 mW. Given that the RIS includes 450 SP4T switches, its total consumption is

merely 100.8 mW. The extremely low power consumption characteristic of the RIS is very attractive for large-scale array applications.

Table 2 compares the performances of the proposed RIS with other referenced designs. It can clearly be observed that the proposed RIS can provide 2-bit phase resolution and dual polarization, outperforming most of the other designs. Compared to Yin et al. (2024)'s design, there are fewer switches in our design, and our power consumption is much lower.

4 Conclusions

In this article, a 2-bit dual-polarized electronic beam scanning RIS is proposed for 6G near-field applications. The element is based on a dual-polarized slot-coupled patch antenna. Each polarization needs only one SP4T switch to generate 2-bit phase quantization. The two orthogonal polarizations are capable of being controlled independently. A 225-element RIS is fabricated and measured. The main beam can scan from −60° to 60° in both *xoz* and *yoz* planes. The measured peak aperture efficiency achieved for the horizontal and vertical polarizations is 40.1% and 38.3%, respectively. With the merits of low cost, low power consumption, dual polarization, and 2-bit phase quantization, the proposed RIS has great potential for use in 6G wireless communications.

Contributors

Xiaowei CAO designed the research. Youjia YIN and Yinan HAO processed the data. Changjiang DENG drafted the paper. Weidong HU, Zhewei FU, and Zhiji DENG helped organize the paper. Changjiang DENG revised and finalized the paper.

Conflict of interest

All the authors declare that they have no conflict of interest.

Data availability

The data that support the findings of this study are available from the corresponding author upon reasonable request.

References

Alexandropoulos GC, Shlezinger N, Alamzadeh I, et al., 2024. Hybrid reconfigurable intelligent metasurfaces: enabling simultaneous tunable reflections and sensing for 6G wireless communications. *IEEE Veh Technol Mag*, 19(1):75-84. https://doi.org/10.1109/MVT.2023.3332580

Dai LL, Wang BC, Wang M, et al., 2020. Reconfigurable intelligent surface-based wireless communications: antenna design, prototyping, and experimental results. *IEEE Access*, 8:45913-45923. https://doi.org/10.1109/ACCESS.2020.2977772

Dai ZY, Xu JR, Zeng Y, et al., 2024. Characterizing the rate region of active and passive communications with RIS-based cell-free symbiotic radio. *IEEE Int Things J*, 11(4):5653-5666. https://doi.org/10.1109/JIOT.2023.3308970

Dash S, Psomas C, Krikidis I, et al., 2022. Active control of THz waves in wireless environments using graphene-based RIS. *IEEE Trans Antenn Propag*, 70(10):8785-8797. https://doi.org/10.1109/TAP.2022.3142272

Feng PY, Qu SW, Yang SW, 2018. Octave bandwidth transmitarrays with a flat gain. *IEEE Trans Antenn Propag*, 66(10):5231-5238. https://doi.org/10.1109/TAP.2018.2858198

Han JQ, Li L, Liu GY, et al., 2019. A wideband 1 bit 12×12 reconfigurable beam-scanning reflectarray: design, fabrication, and measurement. *IEEE Antenn Wirel Propag Lett*, 18(6):1268-1272. https://doi.org/10.1109/LAWP.2019.2914399

Hao YN, Deng CJ, Cao XW, et al., 2024. A high aperture efficiency 1-bit reconfigurable reflectarray antenna with extremely low power consumption. *IEEE Trans Antenn Propag*, 72(1):1015-1020. https://doi.org/10.1109/TAP.2023.3310579

Hum SV, Okoniewski M, Davies RJ, 2007. Modeling and design of electronically tunable reflectarrays. *IEEE Trans Antenn Propag*, 55(8):2200-2210. https://doi.org/10.1109/TAP.2007.902002

Jiang H, Xiong BP, Zhang HM, et al., 2023. Hybrid far- and near-field modeling for reconfigurable intelligent surface assisted V2V channels: a sub-array partition based approach.

Table 2 Comparisons between the proposed design and other RISs

Reference	Frequency (GHz)	Element period (λ_0)	Number of elements	Phase resolution	Polarization	Number of switches per element	Gain (dBi)	AE (%)
Lee et al. (2022)	9.85	0.34	12×12	1-bit	SP	1	17.14	28
Hao et al. (2024)	5.4	0.45	14×14	1-bit	SP	1	21.5	28.5
Xiang et al. (2022)	12.5	0.22	16×16	1-bit	SP	1	20.1	24.0
Dai LL et al. (2020)	2.3	0.38	16×16	2-bit	AP	5	21.7	31.3
Luyen et al. (2020)	10	0.40	24×24	2-bit	AP	4	25.9	39.4
Wang EH et al. (2024)	26.1	0.43	24×24	2-bit	SP	2	29.2	27.1
Yin et al. (2024)	3.6	0.40	16×16	2-bit	DP	4	23.1	40.6
This work	3.6	0.40	15×15	2-bit	DP	2	22.5/22.3	40.1/38.3

SP: single polarization; AP: agile polarization; DP: dual polarization; AE: aperture efficiency. The values in front of and behind the symbol "/" represent the results of horizontal and vertical polarization, respectively

IEEE Trans Wirel Commun, 22(11):8290-8303. https://doi.org/10.1109/TWC.2023.3262063

Jiang YH, Gao FF, Jian MN, et al., 2023. Reconfigurable intelligent surface for near field communications: beamforming and sensing. *IEEE Trans Wirel Commun*, 22(5):3447-3459. https://doi.org/10.1109/TWC.2022.3218531

Kim H, Oh S, Bang S, et al., 2023. Independently polarization manipulable liquid-crystal-based reflective metasurface for 5G reflectarray and reconfigurable intelligent surface. *IEEE Trans Antenn Propag*, 71(8):6606-6616. https://doi.org/10.1109/TAP.2023.3283136

Lee SG, Nam YH, Kim Y, et al., 2022. A wide-angle and high-efficiency reconfigurable reflectarray antenna based on a miniaturized radiating element. *IEEE Access*, 10:103223-103229. https://doi.org/10.1109/ACCESS.2022.3204400

Li P, Yu H, Su JX, et al., 2023. A low-RCS multifunctional shared aperture with wideband reconfigurable reflectarray antenna and tunable scattering characteristic. *IEEE Trans Antenn Propag*, 71(1):621-630. https://doi.org/10.1109/TAP.2022.3225588

Li XR, Lu HQ, Zeng Y, et al., 2022. Near-field modeling and performance analysis of modular extremely large-scale array communications. *IEEE Commun Lett*, 26(7):1529-1533. https://doi.org/10.1109/LCOMM.2022.3172437

Li XY, Wan YL, Liu J, et al., 2021. Broadband electronically scanned reflectarray antenna with liquid crystals. *IEEE Antenn Wirel Propag Lett*, 20(3):396-400. https://doi.org/10.1109/LAWP.2021.3051797

Li ZP, Huo P, Wu Y, et al., 2021. Reflectarray compact antenna test range with controlled aperture disturbance fields. *IEEE Antenn Wirel Propag Lett*, 20(7):1283-1287. https://doi.org/10.1109/LAWP.2021.3077739

Luyen H, Booske JH, Behdad N, 2020. 2-bit phase quantization using mixed polarization-rotation/non-polarization-rotation reflection modes for beam-steerable reflectarrays. *IEEE Trans Antenn Propag*, 68(12):7937-7946. https://doi.org/10.1109/TAP.2020.3000517

Mao YL, Xu SH, Yang F, et al., 2015. A novel phase synthesis approach for wideband reflectarray design. *IEEE Trans Antenn Propag*, 63(9):4189-4193. https://doi.org/10.1109/TAP.2015.2447004

Mei P, Cai Y, Zhao K, et al., 2022. On the study of reconfigurable intelligent surfaces in the near-field region. *IEEE Trans Antenn Propag*, 70(10):8718-8728. https://doi.org/10.1109/TAP.2022.3147533

Moghadas H, Daneshmand M, Mousavi P, 2015. MEMS-tunable half phase gradient partially reflective surface for beam-shaping. *IEEE Trans Antenn Propag*, 63(1):369-373. https://doi.org/10.1109/TAP.2014.2364303

Pan WB, Huang C, Chen P, et al., 2013. A beam steering horn antenna using active frequency selective surface. *IEEE Trans Antenn Propag*, 61(12):6218-6223. https://doi.org/10.1109/TAP.2013.2280592

Perruisseau-Carrier J, 2010. Dual-polarized and polarization-flexible reflective cells with dynamic phase control. *IEEE Trans Antenn Propag*, 58(5):1494-1502. https://doi.org/10.1109/TAP.2010.2044333

Perruisseau-Carrier J, Skrivervik AK, 2008. Monolithic MEMS-based reflectarray cell digitally reconfigurable over a 360° phase range. *IEEE Antenn Wirel Propag Lett*, 7:138-141. https://doi.org/10.1109/LAWP.2008.919327

Vilenskiy AR, Makurin MN, Lee C, et al., 2020. Reconfigurable transmitarray with near-field coupling to gap waveguide array antenna for efficient 2-D beam steering. *IEEE Trans Antenn Propag*, 68(12):7854-7865. https://doi.org/10.1109/TAP.2020.2998904

Wang EH, Peng GY, Zhong KJ, et al., 2024. A 1296-cell reconfigurable reflect-array antenna with 2-bit phase resolution for Ka-band applications. *IEEE Trans Antenn Propag*, 72(4):3425-3437. https://doi.org/10.1109/TAP.2024.3368220

Wang XH, Shu F, Chen RQ, 2023. Beamforming design for RIS-aided amplify-and-forward relay networks. *Front Inform Technol Electron Eng*, 24(12):1728-1738. https://doi.org/10.1631/FITEE.2300118

Wang ZL, Mu XD, Liu YW, 2023. Near-field integrated sensing and communications. *IEEE Commun Lett*, 27(8):2048-2052. https://doi.org/10.1109/LCOMM.2023.3280132

Wu F, Zhao WG, Xia XY, et al., 2023. A 2 bit circularly polarized reconfigurable reflectarray using p-i-n-diode-tuned crossed-bowtie patch elements. *IEEE Trans Antenn Propag*, 71(9):7299-7309. https://doi.org/10.1109/TAP.2023.3291773

Wymeersch H, He JG, Denis B, et al., 2020. Radio localization and mapping with reconfigurable intelligent surfaces: challenges, opportunities, and research directions. *IEEE Veh Technol Mag*, 15(4):52-61. https://doi.org/10.1109/MVT.2020.3023682

Xiang BJ, Dai X, Luk KM, 2022. A wideband low-cost reconfigurable reflectarray antenna with 1-bit resolution. *IEEE Trans Antenn Propag*, 70(9):7439-7447. https://doi.org/10.1109/TAP.2022.3176868

Xu DN, Han Y, Li X, et al., 2023. Energy efficiency optimization for a RIS-assisted multi-cell communication system based on a practical RIS power consumption model. *Front Inform Technol Electron Eng*, 24(12):1717-1727. https://doi.org/10.1631/FITEE.2300136

Xu HJ, Xu SH, Yang F, et al., 2020. Design and experiment of a dual-band 1 bit reconfigurable reflectarray antenna with independent large-angle beam scanning capability. *IEEE Antenn Wirel Propag Lett*, 19(11):1896-1900. https://doi.org/10.1109/LAWP.2020.3011578

Xu JQ, Mu XD, Liu YW, 2024. Exploiting STAR-RISs in near-field communications. *IEEE Trans Wirel Commun*, 23(3):2181-2196. https://doi.org/10.1109/TWC.2023.3296191

Yang HH, Yang F, Xu SH, et al., 2017. A study of phase quantization effects for reconfigurable reflectarray antennas. *IEEE Antenn Wirel Propag Lett*, 16:302-305. https://doi.org/10.1109/LAWP.2016.2574118

Yin YJ, Deng CJ, Cao XW, et al., 2024. Design of a 2-bit dual-polarized reconfigurable reflectarray with high aperture efficiency. *IEEE Trans Antenn Propag*, 72(1):542-552. https://doi.org/10.1109/TAP.2023.3326951

Zhang QS, Zhang MT, Shi XW, et al., 2022. A low-profile beam-steering reflectarray with integrated leaky-wave feed and 2-bit phase resolution for Ka-band SatCom. *IEEE Trans Antenn Propag*, 70(3):1884-1894. https://doi.org/10.1109/TAP.2021.3111172

Zhang X, Zhang HY, 2023. Hybrid reconfigurable intelligent surfaces-assisted near-field localization. *IEEE Commun Lett*, 27(1):135-139. https://doi.org/10.1109/LCOMM.2022.3215253

Zhao YJ, 2023. Reconfigurable intelligent surfaces for 6G: applications, challenges, and solutions. *Front Inform Technol Electron Eng*, 24(12):1669-1688. https://doi.org/10.1631/FITEE.2200666